



Simon Vella

Department of Mechanical Engineering,
University of Bath,
Bath BA2 7AY, UK

Hui Tang

Department of Mechanical Engineering,
University of Bath,
Bath BA2 7AY, UK

Mauro Carnevale

Department of Mechanical Engineering,
University of Bath,
Bath BA2 7AY, UK

James A. Scobie

Department of Mechanical Engineering,
University of Bath,
Bath BA2 7AY, UK

Gary D. Lock

Department of Mechanical Engineering,
University of Bath,
Bath BA2 7AY, UK

Francesco Salvatori

Safran Aircraft Engines,
Villaroche, Moissy-Cramayel 77550, France

Carl M. Sangan¹

Department of Mechanical Engineering,
University of Bath,
Bath BA2 7AY, UK
e-mail: c.m.sangan@bath.ac.uk

On the Relationship Between Swirl and Unsteadiness Within Turbine Rim Seals

Unraveling the flow physics pertaining to hot gas ingress in turbines is crucial in enabling designers to realize global decarbonization targets in aerospace. A turbine rim seal is fitted at the periphery of the rotor–stator cavity to minimize the ingress of annulus gas, which detrimentally affects cycle’s efficiency. The inherent unsteadiness in rim seal flows, arising from shear gradients between contiguous flow paths, introduces a consequential, yet presently unestablished, influence on sealing characteristics. A single-stage axial turbine facility in conjunction with an aeroengine architecture is employed to assess the steady and unsteady sealing characteristics of a range of industrially relevant rim seals. Time-averaged measurements of gas concentration and swirl, acquired over a range of flow coefficients (C_F), exhibited an inverse relationship between sealing performance and the purge-mainstream swirl difference ($\Delta\beta$). Spectral analysis of unsteady pressure signals revealed an associated unsteadiness, induced by the strength of the annulus-cavity interaction. Across all C_F , a low-frequency harmonic range consistently displayed proportionality between spectral activity and $\Delta\beta$. Thus, a relationship between steady and unsteady characteristics was established. Examining a series of rim seal configurations with varying radial clearances signified that sealing performance was predominantly influenced by the radially outermost clearance. The configurations exhibiting superior performance presented heightened spectral activity, ascribed to an increased radial purge mass flux and establishing a definite relationship with concurrent steady measurements.

[DOI: 10.1115/1.4066997]

Keywords: aeroengine turbine rim seals, turbulent flows, spectral analysis, cavity flows, clearance changes

1 Introduction

Global decarbonization presents a significant challenge for the aeroengine designer. Aeroengine efficiency can be increased by raising the turbine entry temperature; high turbine entry temperatures demand cooling of the turbine components and hence optimized rim seal design. A turbine rim seal is fitted at the periphery of the wheel-space, formed between adjacent stator and rotor disks. High pressure air is typically bled from the compressor and reintroduced in the turbine to pressurize the cavities and limit hot gas ingress from the mainstream gas path. Insufficient purge air could potentially lead to catastrophic engine failure, yet superfluous use of purge has a parasitic effect upon engine efficiency.

The fluid mechanics occurring in rim seal flows are complex due to the existence of inherent unsteadiness, dominated by the formation of large-scale unsteady structures that are yet to be

convincingly delineated in the context of sealing performance. The upstream wheel-space in Fig. 1 illustrates the characteristic flow features within a generic turbine rim seal. Current research has demonstrated the existence of six primary drivers for ingress: (a) annulus pressure field asymmetries, typically referred to in the literature as externally induced mechanisms; (b) disk pumping, related to rotationally induced entrainment; (c) shear-driven instabilities arising due to the radial gradient in velocity between contiguous flow paths; (d) turbulent diffusion between the mainstream and cavity; (e) inertial waves driven by the Coriolis force; (f) acoustic effects and cavity modes.

It is well-established that ingress drivers are fundamentally related to the mainstream flow coefficient (and therefore the annulus swirl), purge mass flowrate, and rim seal geometry. However, the direct impact of these parameters upon the unsteadiness within the system remains largely unexplained. The wider literature contains much discussion of the steady implications for ingress, yet the interdependency of the unsteady drivers is seldom explored. The latter is critical when associating sealing effectiveness with unsteady characteristics.

¹Turbo Expo, June 24–28, 2024. GT2024.

¹Corresponding author.

Manuscript received September 16, 2024; final manuscript received October 14, 2024; published online December 11, 2024. Editor: Jerzy T. Sawicki.

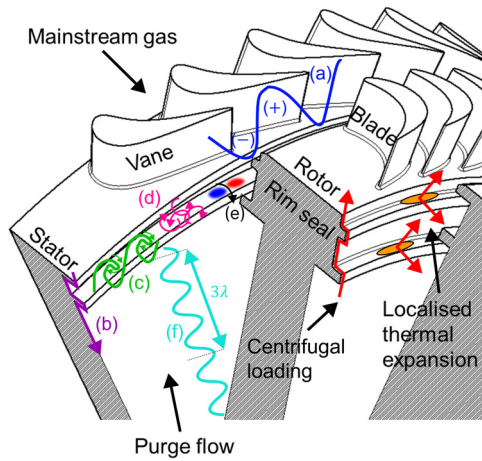


Fig. 1 Schematic of a typical gas turbine stage. Instability mechanisms are highlighted in the upstream cavity; transient events resulting in clearance changes are annotated for the downstream cavity.

Comparison of the inherent unsteadiness (typically limited to an idealized rotating structure count and speed) is often reported for rim seal geometries, without consideration for the impact of clearance change; rim seal clearances change during operation subject to aeroengine transients. As highlighted in the downstream wheel-space of Fig. 1, causes for such variation include: thermal expansion and centrifugal loading on the rotating disks. A direct link between unsteadiness and rim seal clearance is key to predicting sealing performance over the operational envelope of the engine.

1.1 Instability Mechanisms. The presence of circumferential nonuniformities (often characterized as rotating structures) in a rotor–stator system was first demonstrated by Cao et al. [1], both experimentally and computationally. The strength of the vortical structures was a function of the rim seal clearance, whereby a reduction in clearance corresponded to reduced unsteadiness and therefore a weakening of the relative impact of the structures. Determining the driving mechanism for the creation of such instabilities remains a prevailing aspect of current ingress research. The literature reports a wide range of physical mechanisms that result in the production of unsteady structures, originating from viscous or inviscid effects.

Savov et al. [2] conducted an experimental investigation to directly compare the unsteady characteristics of a single and double lip seal. The single lip seal was shown to be sensitive to the unsteady blade pressure field. The presence of rotor blades acted to suppress spectral activity, particularly at smaller superposed flow rates. Spectral activity intensified with increased purge flowrate, which was attributed to the relative increase in the shear, i.e., a viscous effect. Pressure fluctuations were largest in proximity to the mainstream flow, indicating that the unsteadiness originated from the mainstream gas path. However, the impact of such fluctuations on ingress remains largely unknown.

Unsteadiness originating from the gas path was investigated both experimentally and computationally by Monge-Concepción et al. [3], through analysis of the impact of vane trailing-edge flow upon the rim seal flow-field. The number of structures in the rim seal increased as the cavity pressurized, with a subsequent reduction in rotational speed. It was postulated that this increased number of instabilities was due to a strengthened purge-mainstream shear gradient.

The characterization of large-scale instabilities during transient conditions was examined by Rozman et al. [4]. Time-resolved measurements demonstrated that a sensitivity exists between the dominant frequency of rim seal unsteadiness and the superposed purge flowrate. However, an independence was also observed

between this frequency and the disk speed; it was suggested that this demonstrated the relative dominance of shear effects over inertial contributions.

The advent of high-performance computing and availability of nonintrusive fast-response probes (as employed in Refs. [2–4]) has led to an increase in the number of proposed inviscid mechanisms for ingress. The experiments of Berg et al. [5] provided preliminary evidence for the presence of Helmholtz and acoustic modes in the rotor–stator cavity. Unsteady pressure sensors were installed in both the rotor and stator disks. However, it was noted that much of the measured unsteady data was too noisy to provide any useful information. Furthermore, it was demonstrated that the background frequencies (i.e., electrical noise when the rig was stationary) overlapped with those hypothesized to demonstrate acoustic modes. Hösgen et al. [6] performed 360 deg a large eddy simulation (LES) of an axial seal and suggested that coherent structures were produced by the excitation of acoustic modes, driven extensively by oscillations in the pressure signal within the turbine rim seal.

Bru Revert et al. [7] examined the unsteady rim seal pressure field for differing annulus flow conditions. In the absence of annulus flow, spectral content was centered at a frequency primarily dictated by disk rotation. The authors associated these structures with inertial waves, as originally suggested by Gao et al. [8]. Following the introduction of a swirled annulus flow, an energetic region was excited related to shear, in addition to the weakened inertial wave frequency band.

Considering the breadth of experimental data available in the literature, a clear correlation between the principal drivers for ingress and intrinsic unsteadiness is yet to be established. It is currently postulated that resultant instabilities are a transport mechanism for ingress; however, without clear correlation to sealing performance, this postulation remains unsubstantiated.

1.2 Effect of Rim Seal Geometry. Comparisons of alternate rim seal configurations are prevalent in the literature, yet controlled parametric studies of a consistent seal architecture are lacking. Experimental campaigns have classically focused upon the characterization of discrete rim seal configurations through the assessment of sealing effectiveness across a range of purge flow rates and mainstream flow coefficients.

The implications of geometric features were experimentally studied by Sangan et al. [9], who directly compared the *steady* performance of generic rim seals. Measurements of sealing effectiveness demonstrated that a single radial lip substantially improved sealing characteristics relative to a baseline axial seal. A further improvement was obtained by using a second radial lip (hence double lip seal), which acted to confine ingested fluid to the outer wheel-space.

Popović et al. [10] conducted a computational study utilizing a steady Reynolds-Averaged Navier–Stokes (RANS) methodology to quantify the effects of parametric variations within a simplified rim seal geometry. A baseline configuration was displaced radially and axially, resulting in compound changes of seal clearance. It was concluded that tightening the seal clearance in closest proximity to the annulus offered an improvement in sealing performance. Results were in agreement with the experimental investigation of Daniels et al. [11], who demonstrated a significant improvement in sealing effectiveness upon decreasing the outermost radial clearance.

The effect of geometric modification in close proximity to the annulus was further demonstrated by Burden et al. [12]. A series of Wall Modeled LES completed under rotationally induced conditions demonstrated that substantial benefits could be obtained by increasing the ratio of the flow length within the seal as a fraction of seal compactness.

1.3 Influence of Swirl Upon Ingress. Through a series of direct measurements of annulus swirl using an aerodynamic probe, Graikos et al. [13] directly collapsed rim seal effectiveness with purge-mainstream swirl difference. This offered an initial indication

that the purge-mainstream swirl difference was a principal driver for rim seal performance.

Choi et al. [14] furthered this line of enquiry by experimentally investigating the impact of a rotor-side impeller in the wheel-space of the rotor–stator cavity flow field. The *swirler* was found to reduce the minimum purge mass flow required to seal the cavity; no assessment of the windage penalty was provided for context to this potential benefit.

An Unsteady RANS approach was utilized by Cong et al. [15] to examine the impact of the absolute flow angle at the vane exit upon local sealing effectiveness. The presence of reduced swirl in proximity to the hub was found to produce a substantial increase in sealing performance when assessed on both the stator and rotor-side of the wheel-space.

A definitive relationship between the inherent unsteadiness associated with rim seal flows and time-averaged sealing performance is yet to be established. The strategy employed in this paper was to independently investigate the impact of known ingress drivers upon the spectral characteristics of an aeroengine representative rim seal. Time-averaged measurements of swirl and concentration were combined with spectral analysis of unsteady pressure signals to elucidate a direct association between steady and unsteady modes for ingress.

2 Experimental Facility

The one-stage turbine facility at the University of Bath models ingress into an aeroengine representative wheel-space formed between an adjacent stator and rotor disk (Fig. 2). A Safran Aircraft Engines (SAE) rim seal geometry was fitted to the wheel-space. The rig operates under fluid-dynamically scaled conditions at an engine-representative C_F with a rotational Reynolds number up to 10^6 and vane exit Mach number 0.32. A complete description of the facility, its instrumentation and measurement locations are provided by Vella et al. [16].

The single-stage turbine consists of a stator with 28 vanes and a rotor blisc featuring 56 symmetric rotor blades. The rig facilitates a modular design where both stator-side and rotor-side wheel-space geometries and clearances can be modified expediently.

A gas concentration technique was used to quantify ingress from the annulus into the wheel-space; superposed purge flow was seeded with a tracer gas: $\sim 1\%$ CO_2 . The sealing effectiveness (ϵ_c) is defined as

$$\epsilon_c = \frac{c_s - c_a}{c_0 - c_a} \quad (1)$$

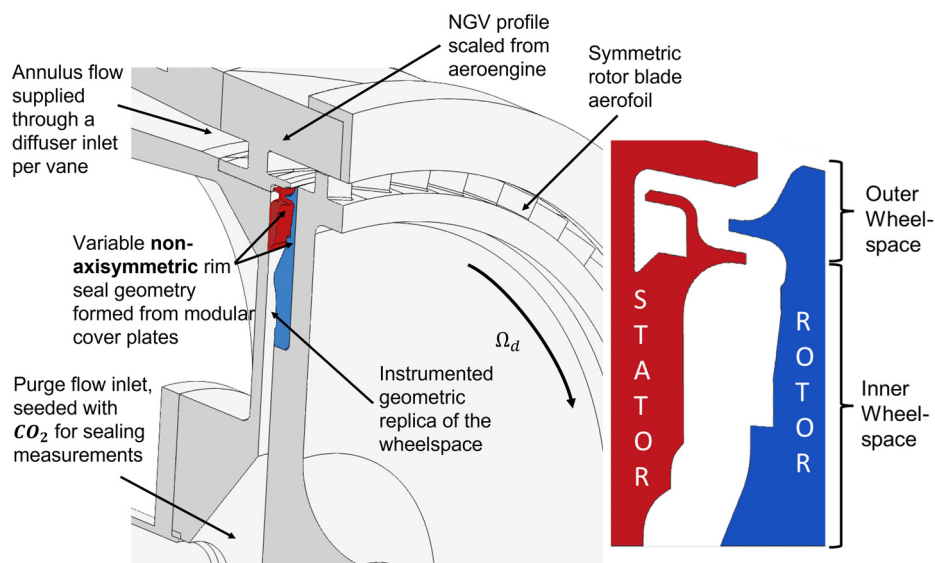


Fig. 2 One-stage turbine facility highlighting the test cavity. Variable stator and rotor-side cover plates allow for interchangeable cavity geometry and rim seals.

where c_s is the local CO_2 concentration, normalized by measurements in the annulus (subscript a) and in the purge supply (subscript 0). CO_2 concentration was measured using a Signal Group 9000MGA multigas analyzer, connected to a 20-channel multiplexor.

Pitot probes aligned to the tangential direction were fitted 2.7 mm proud of the stator disk, with corresponding static taps on the stator surface between $0.4 \leq r/b \leq 0.93$. A 48-channel Scanivalve permitted the simultaneous assessment of the radial distribution of static and total pressures. The local swirl ratio is defined as follows:

$$\beta = \frac{V_{\phi\infty}}{\Omega r} \quad (2)$$

where the tangential component of velocity in the core, $V_{\phi\infty}$, was calculated through Bernoulli's principle.

Purge flow was introduced at a low radius through the bore of the wheel-space. A Bronkhorst thermal mass flowmeter was coupled with control valves to measure and control the supply of purge flow. The mass flowmeter was accurate up to $\pm 0.2\%$ of the 0.073 kg/s full-scale range and maintained linearity at the minimal flow rates.

A normalized nondimensional purge flow parameter is defined as $\bar{\Phi}_0$

$$\bar{\Phi}_0 = \frac{\Phi_0}{\Phi_{0,\min^*}} \quad (3)$$

where

$$\Phi_0 = \frac{\dot{m}_0}{2\pi s_c \rho \Omega b^2} \quad (4)$$

Φ_{0,\min^*} is the minimum purge flow required to seal the wheel-space for the Baseline configuration. Therefore, Φ_{0,\min^*} is the value of Φ_0 where $\epsilon_c = 1$ at $r/b = 0.93$ (see Sec. 2.2) inside the inner wheel-space, where b is taken to be the minimum radial extent of the nonaxisymmetric underside of the stator shroud (Fig. 3) [16].

2.1 Operating Conditions. The operating conditions at the design point are summarized in Table 1. Parameters were tuned to ensure a constant $C_F = 0.51$ for all “on-design” experiments reported here.

2.2 Baseline Aeroengine Representative Seal and Geometry Matrix. Figure 3 presents the main features of the aeroengine representative Baseline rim seal geometry. The double seal divides

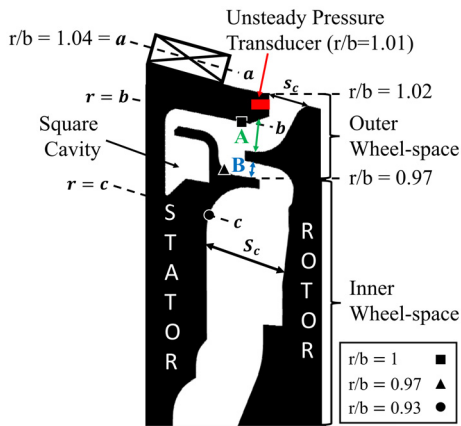


Fig. 3 Cross section of the aeroengine representative rim seal. Silhouettes are skewed to comply with confidentiality agreements with SAE. The stage consists of a cylindrical annulus. Clearances investigated within this study have been defined as Clearances A and B.

the wheel-space into two distinct regions: an inner and outer wheel-space. The configuration includes features such as complex rotor-side curvature and an omega-seal cover plate on the stator side.

The modularity of the facility (highlighted in Fig. 2) was exploited to isolate an inner and outer radial clearance, denoted Clearances A and B in Fig. 3. These clearances were varied to obtain the seal configurations examined in this study. The rim seal geometry is constructed through the interface of three components: the nozzle guide vane, a stator-side cover plate, and a rotor-side coverplate. Several rotor and stator-side cover plates were commissioned to permit the variation of the discrete clearances under investigation, while maintaining the geometrical consistency of the remaining rim seal geometry and nozzle guide vane under-shroud design.

Rotor-side cover plates were specifically designed to model radial changes in displacement whilst preserving a consistent annulus line. Geometric blending was used to preserve the rake angle and therefore inner curvature of the rotor-side fin. Only the outermost ($\leq 0.3\%$) of the radial extent of the wheel-space is affected by geometric blending. Adopting a phased methodology to investigate clearance variation isolated a single clearance displacement that might occur within an engine operational transient. The axial clearance at the periphery of the wheel-space ($r/b = 1.02$), is constant for all configurations; the constant s_c is used to determine Φ_0 throughout this study.

An illustration of the range of geometries investigated is presented in Fig. 4. The extent of Clearance A was perturbed by $\pm 18\%$ with respect to the Baseline configuration, while Clearance B was altered by $\pm 33\%$. Furthermore, two compound configurations were evaluated whereby Clearance A was decreased by 18%, while Clearance B was simultaneously increased by 33%, and *vice versa* to simulate the other extremity. Compound tests model the impact of

Table 1 Operating conditions at the design point

Parameters	
Rotational Reynolds number (Re_ϕ)	8.9×10^5
Axial-flow Reynolds number (Re_w)	4.6×10^5
Flow coefficient (C_F)	0.51
Vane exit Mach number (M)	0.32

centrifugal loading displacing the complete rotor disk, while assessment of individual clearances is indicative of the influence of localized seal tip displacement, which occurs on both rotor-side and stator-side components.

The centrifugal growth of the rotor-side seal lip was measured with a micro-epsilon opto NCDT 1402 LASER when subject to disk rotation. The maximum radial displacement of the seal lip was equal to 3.5% of Clearance B; or 5.2% of Clearance B when $B_{\min} = B - 33\%$.

2.3 Unsteady Pressure Measurements. To characterize the inherent unsteadiness within the rim seal configurations, two Kulite XCQ-062 absolute pressure transducers were positioned at $r/b = 1.01$ in the rim gap (Fig. 3). Sensors were spaced at an angle of 12.9 deg, equivalent to one vane pitch, and mounted flush to the stator-side surface. The selection of the sensor was driven by the passing frequency of the blade (BPF) at $Re_\phi = 8.9 \times 10^5$. This was substantially lower (3.27 kHz) than the natural frequency of the sensor (150 kHz). The stated manufacturing uncertainty associated with the transducers is $\pm 0.1\%$ of the full-scale (350 mbar), inclusive of nonlinearity, hysteresis, and repeatability.

The data acquisition system was specifically designed to shield unsteady pressure signals, owing to the sensitivity of the associated instrumentation—highlighted in Berg et al. [5]. A 12 V DC battery was used to power the system, minimizing the inherent electrical noise associated with the three-phase power supply used to drive the motor.

The two sensor channels were measured in parallel using an NI 9205 CompactDAQ data platform. A 100 kHz sampling frequency was selected to maximize signal resolution and hence reduce the potential overlap of frequency components. This ensured a Nyquist frequency that was far from the area of interest considering the frequency domain. All pressure signals were recorded for 10-s intervals, corresponding to 583 complete rotor revolutions at the nominal design speed.

3 Unsteady Data Processing

Although contemporary understanding widely accepts the inevitable role of rotating instabilities within the ingress problem, a convincing association between the two has not been established. The subjectivity associated with identifying the true coherence from time-resolved pressure signals hinders research in this area. Measured signals contain an amalgamation of physical phenomena;

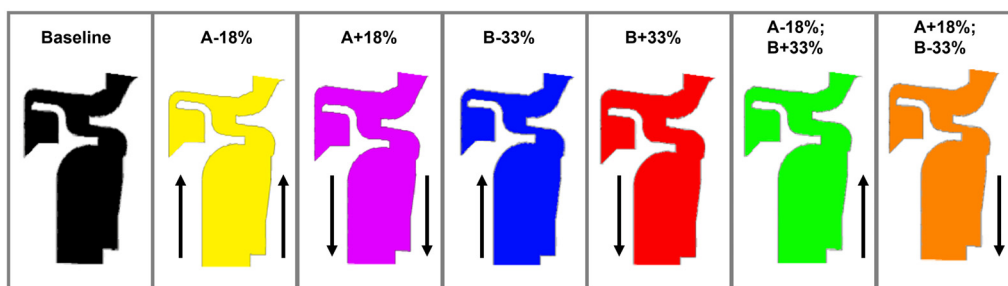


Fig. 4 Examined rim seal configurations with annotated displacements of rotor and stator coverplates relative to the Baseline. Geometries are identified with respect to variations of Clearances A and B.

discerning governing contributions to ingress must be considered within analysis methods.

3.1 Isolation of Stochastic Contribution. Considerable spectral activity in the low-frequency band is typical of most datasets found in the open literature, often attributed to different origins yet consistently removed from onward analysis, as measurements were thought to be nonphysical. Bru Revert et al. [7] associated this band to rotor eccentricity, while Camci et al. [17] postulated that this low-frequency excitation was a result of electrical noise interfering with measurements. However, any form of rigorous definition or mathematical formulation enabling a robust identification of nonphysical frequency bands has yet to be provided.

To facilitate a robust definition of stochastic elements in measured unsteady pressure signals, a discrete wavelet transform (DWT) algorithm was employed, due to its ability to analyze and represent a signal in the frequency domain at different scales. DWT can be considered as an adaptable high-pass filter that is informed by the physical characteristics of the signal. Stochastic or *noisy* components of a signal classically exhibit fluctuations at smaller scales (i.e., temporal or spatial intervals within which fluctuations occur) relative to that of the deterministic aspect of the signal. The decomposition of a signal utilizing a DWT algorithm requires the high-pass filter characteristics of the wavelet function to isolate frequency components at a higher scale or level within the wavelet decomposition, classically associated with stochastic elements. The orthogonal *Daubechies 5 waveform (db5)* [18] was chosen as the mother wavelet for this study as it exhibited a similar shape to the measured signal shape. Six decomposition levels were used throughout this analysis to ensure adequate resolution in the frequency domain. The algorithm effectively isolates DWT coefficients associated with the high-frequencies representative of the stochastic contribution. The signal can thus be reconstructed utilizing modified coefficients, obtaining a representative, yet filtered, signal without stochastic elements.

Figure 5 presents an example exploitation of this algorithm. A discrete Fourier transform (DFT) has been performed on both the original and modified unsteady pressure signals, highlighting the stochastic contribution at the low-frequency band; clear peaks are seen at $f/f_d < \sim 10$ ($f < \sim 580$ Hz), which are discarded from further analysis due to their nondeterministic origin. Conservative thresholding enables the stochastic contribution at higher frequencies to remain. This process ensures that any physical interactions occurring in a frequency interval coinciding with such electrical excitation are not erroneously removed from the signal.

3.2 Ensemble-Averaged Power Spectral Density. The DFT technique is practical when analyzing pressure signals containing a finite number of dominant frequencies. However, rim seal flows can be highly unsteady and unstable, especially in close proximity to the

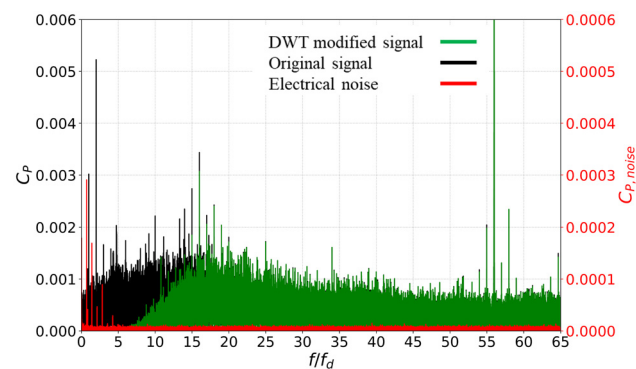


Fig. 5 Discrete Fourier transform analysis for the Baseline seal at the “on-design” condition, demonstrating the DWT algorithm removing stochastic contribution: $\Phi_0=1.34$. The secondary ordinate corresponds to a C_p concerned with background frequencies (i.e., electrical noise when the rig was stationary).

annulus, requiring signal analysis to be conducted over larger temporal intervals where DFT analysis is prone to amplitude suppression. Unsteadiness is a phenomenon frequently encountered in the analysis of dynamic systems. Power spectral density (PSD) characterizes the distribution of signal power across different frequencies, enabling insight into the temporal dynamics of a given signal. PSD produces a continuous frequency spectrum indicative of the evolution of the power with time (i.e., capturing transient behavior), while attenuating the spectral noise associated with DFT bins.

In instances where an elevated unsteadiness is observed, an increased PSD manifests itself as a heightened concentration of signal power and therefore energy transfer, in some instances dispersed across a broader range of frequencies. The relationship between unsteadiness and increased PSD demonstrates the potential of PSD analysis as a tool for characterizing temporal dynamics in fluid mechanics.

Power spectral density was determined using Welch’s method [19] with 4000 data points per DFT block, windowed using the Hann algorithm and equal to 2.33 rotor revolutions per periodogram—thus ensuring adequate resolution in both frequency and time domains. This output enabled an ensemble-averaged PSD derived from the measured unsteady pressure fluctuation ($p - \bar{p}$) to be determined. Ensemble averaging was performed over 300 rotor revolutions to capture transient behavior while ensuring that a definitive periodic state was reached. The ensemble-averaged PSD was determined from the spatially averaged signal across the two sensors, to enhance the signal-to-noise ratio. The resultant PSD is, therefore, a characteristic spectral trace representative of the statistical distribution of energy fluctuations at the test condition, and hence the systematic unsteadiness.

4 Results

4.1 Unsteadiness and Ingress. The principal variables that influence ingress in the steady sense are well-established: C_F , Φ_0 , and rim seal geometry. However, unsteady drivers for ingress—and more importantly their relationship—are less well understood.

4.1.1 Influence of C_F . The flow physics occurring in rotor–stator systems are strongly influenced by annulus conditions. Savov et al. [2] demonstrated that the pressure fluctuations governing rim seal unsteadiness originate from the annulus, where high Reynolds number mainstream flow is swirled by the vane exit angle.

Figure 6(a) demonstrates a sensitivity study for C_F at fixed Re_ϕ for the Baseline rim seal geometry. Here, the sealing effectiveness is plotted as a function of the swirl in the annulus; the secondary ordinate indicates the corresponding purge-mainstream swirl difference. The impact of annulus swirl upon sealing performance and unsteadiness was measured concurrently at $\Phi_0 = 0.67$. Sealing effectiveness was evaluated at $r/b = 1$. Sealing effectiveness and swirl in the inner wheel-space were measured at $r/b = 0.93 = c$ across a range of C_F ; at $\Phi_0 = 0.67$. The corresponding swirl was found to remain sensibly constant and equal to $\beta_c \approx 0.4$ across all examined C_F ; the wheel-space remained near-sealed for all C_F at this value of Φ_0 . As a result, $\Delta\beta$ can be evaluated as $\Delta\beta = \beta_a - \beta_c$, where β_a was estimated from isentropic velocity triangles at $r = a$ (see Fig. 3). As $\Delta\beta$ is quantified over a constant radial extent ($\Delta r = a - c$) throughout the duration of this study, $\Delta\beta$ can be considered representative of the purge-mainstream swirl gradient, $\partial\beta$.

As C_F is increased, a monotonic decrease in sealing effectiveness was observed in a manner inversely proportional to $\Delta\beta$ (Fig. 6(a)). This provides evidence that the swirl gradient influences ingress at a constant Φ_0 , consistent with the bladeless case presented by Graikos et al. [20]. Beyond $C_F = 0.50$, although ε_c maintains inverse proportionality to $\Delta\beta$, $\partial\varepsilon_c/\partial\beta_a$ is reduced.

The distribution of spectral power across the frequency domain within the rim seal gap is shown across several values of C_F in

Fig. 6(b). Selected points are indicated by dashed vertical lines and color-coordinated with Fig. 6(a). Two distinct harmonic ranges of increased spectral activity were observed across the frequency domain: a lower frequency contribution ($10 \leq f/f_d \leq 45$) and a higher frequency contribution originating from the BPF ($f/f_d > 45$).

- **Lower-frequency contribution:** The lower-frequency activity is governed by $\Delta\beta$ (Fig. 6(b)) yielding a proportional relationship with the PSD magnitude. The band of spectral activity is contained within a constant harmonic interval indicating proportionality between PSD and β_a , despite the peak within the interval shifting toward a higher frequency as C_F is increased. Shear instabilities arise from velocity gradients between contiguous fluid layers, which, as seen in Fig. 6(b), intensifies with C_F ; this leads to the propagation of instabilities and results in increased unsteadiness. As $\Delta\beta$ is increased, the resultant shear gradient manifests itself as an increased PSD, encouraging ingress penetration into the cavity, transported via large-scale structures (assuming a constant rate of egress).
- **Higher-frequency contribution:** Dissimilar to the spectral contribution associated with $\Delta\beta$, the higher frequency activity near the BPF is not persistent for all C_F (Fig. 6(b)), but rather $C_F \geq 0.45$. It is evident from Fig. 6(b) that spectral peaks originate from the blades due to the relative centering of the BPF within the higher frequency range. Measured nonlinear subharmonics of the BPF have a clear amplitude-threshold dependence, a function of the unsteady pressure fluctuations resulting from blade rotation.

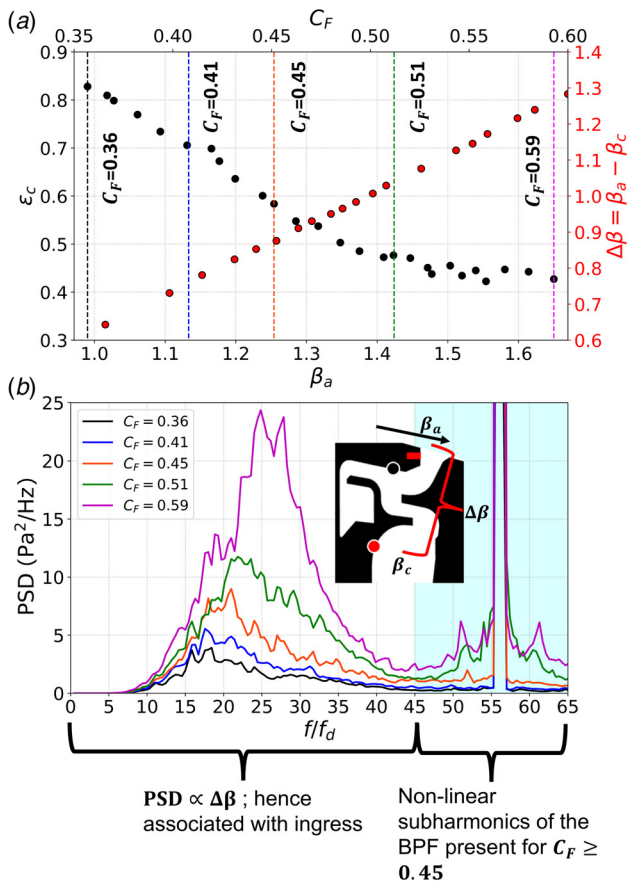


Fig. 6 (a) The variation of sealing performance (at $r/b = 1$) and $\Delta\beta$ with C_F , at a constant $\bar{\Phi}_0 = 0.67$. β_a has been estimated using isentropic velocity triangles, and β_c measured at $r/b = 0.93$. Vertical dashed line highlight C_F values extracted for unsteady analysis. (b) Ensemble-averaged spectral activity across a range of C_F .

Due to its recurrence for all C_F conditions (Fig. 6) the low-frequency, shear-driven unsteadiness associated with the annulus swirl is the dominant ingress mechanism.

4.1.2 *Impact of $\bar{\Phi}_0$.* Consider on-design conditions (Table 1) for the Baseline configuration. Figure 7 presents the effect of superposed flowrate upon sealing performance and spectral content. Sealing effectiveness was measured at three radial locations: $r/b = 0.93$, $r/b = 0.97$, and $r/b = 1$ (Fig. 7(a)). The introduction of purge acts to pressurize the cavity; hence at a $\bar{\Phi}_0 = 0$ the cavity experiences the most significant ingress. As $\bar{\Phi}_0$ is increased the wheel-space begins to pressurize, first in the inner and then the outer wheel-space. The outermost measurement location ($r/b = 1$) does not completely seal throughout the examined range of $\bar{\Phi}_0$.

The unsteady activity for four discrete purge mass flow rates was evaluated, as presented in Fig. 7. As β_a and Re_ϕ are constant, the only parameter modifying unsteadiness is the purge mass flowrate. Increasing $\bar{\Phi}_0$ primarily modifies the lower-frequency contribution, previously identified as resulting from the purge-mainstream shear gradient. Considering first $\bar{\Phi}_0 = 0$, where the cavity experiences the most significant ingress, β_c is closest to β_a so that $\Delta\beta = \Delta\beta_{\min}$ and therefore the annulus flow has the greatest impact upon the rim seal. Perhaps counterintuitively, this condition corresponds to the minimum spectral activity across the low-frequency range (Fig. 7(b)). The tangential velocity difference (ΔV_ϕ) and therefore the shear layer across the rim seal cavity is hence minimized, caused by the deep penetration of ingress.

A critical distinction must be defined in order to address an apparent paradox. Figure 8 demonstrates the implications of varying C_F and $\bar{\Phi}_0$ at a constant disk speed upon the relative flow velocity within the rim seal. First, an increase in C_F at constant $\bar{\Phi}_0$ enhances ΔV_ϕ in proportion to β_a (Fig. 8(a)). Second, increasing $\bar{\Phi}_0$ at constant C_F amplifies ΔV_ϕ in accordance with a reduction in β_c , as demonstrated experimentally and presented in Fig. 7(a). As the wheel-space is pressurized through the superposition of purge flow, the penetration of annulus gas is reduced and the rotating core in the

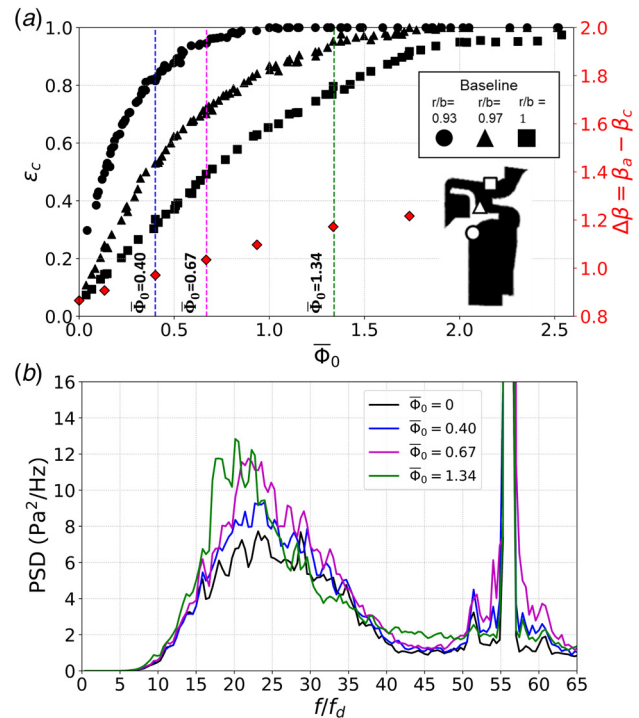


Fig. 7 (a) ϵ_c versus $\bar{\Phi}_0$ curve characterizing sealing performance of the Baseline configuration. Values of $\Delta\beta$ are presented against a secondary ordinate. (b) Ensemble-averaged PSD for the Baseline configuration at design condition, demonstrating the impact of $\bar{\Phi}_0$ upon unsteadiness.

wheel-space is suppressed. Therefore, $\beta_c \rightarrow 0$ so $\Delta\beta \rightarrow \beta_a$ as increased purge is applied as demonstrated in Fig. 8(b). As a result—and recalling Fig. 8— r_m reduces leading to an increase in $\Delta\beta = \Delta\beta/r_m$ and resulting in the observed maximized unsteadiness. The region of maximized spectral activity moves radially outboard as the superposed flowrate, and therefore radial flux of purge, increases. Therefore, considering Fig. 7(a), for $\bar{\Phi}_0 \geq 2.0$ as $r_m \rightarrow 0$ and $\Delta\beta \rightarrow \infty$ a strengthened shear gradient acts across an infinitesimally small radial extent. Relative fluctuations in tangential velocity result in perturbations in the cavity purge flow. Hence, instabilities are promoted, which transport ingress and prevent the complete sealing at the outermost rim seal location.

In a turbulent fluid, the shear gradient promotes both the generation and persistence of eddies at various scales. The process of eddy interaction is commonly referred to as the energy cascade [21]. When the shear gradient increases, independent of the mechanism from which it originates (Fig. 8), it signifies a heightened availability of energy for the cascade, leading to increased energy transfer from larger to smaller eddies. The lower-frequency contribution, shown to be governed by the shear gradient, acts within a constant harmonic interval ($10 \leq f/f_d \leq 45$) across all conditions. The formation of a stable frequency interval indicates an organized pattern of energy transfer.

4.2 Impact of Rim Seal Geometry. Parametric studies of clearance changes while maintaining a consistent seal configuration remain largely unstudied. The effect of radial clearance has been

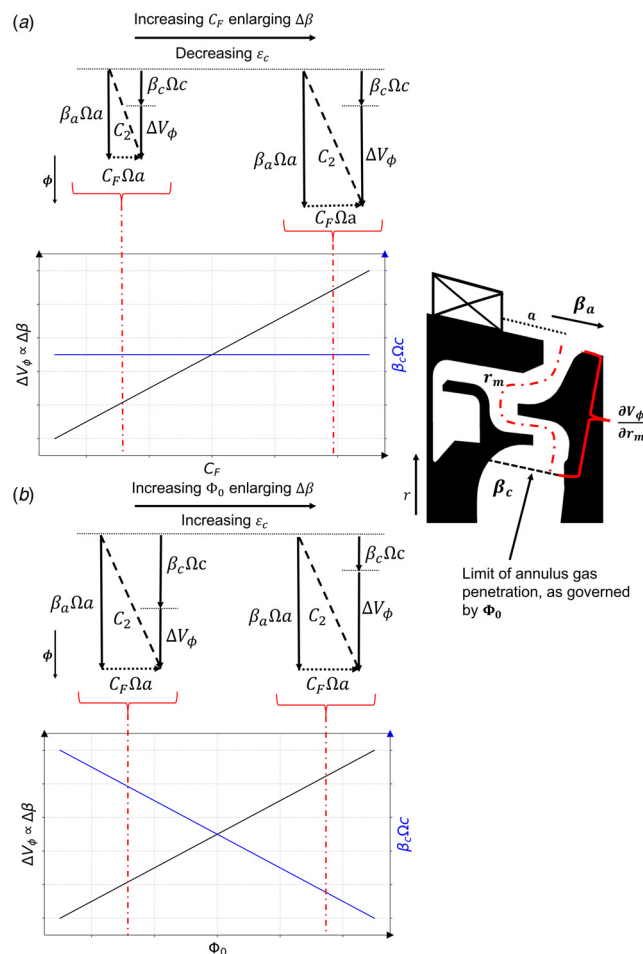


Fig. 8 The effect of C_F and $\bar{\Phi}_0$ upon relative flow velocity within the rim seal cavity, governed by $\frac{\partial V_\phi}{\partial r_m} \propto \Delta V_\phi$ and therefore $\Delta\beta$. r_m is the medial length through the rim seal over which the swirl gradient is evaluated.

investigated here by employing time-averaged and unsteady analysis methods, while maintaining constant on-design conditions throughout (Table 1). Although ϵ_c was evaluated at the $r/b = 0.97$ measurement location for all configurations, it has not been presented herein for conciseness.

4.2.1 Modification of Outermost Radial Clearance. Clearance A has been modified by simultaneously displacing both stator and rotor side geometries by the same radial distance, therefore maintaining a constant Clearance B. The impact of altering the outermost radial clearance (Clearance A) was examined across a range of purge mass flow rates, enabling the characterization of time-averaged, steady sealing performance across the full extent of rim seal flow conditions. Figure 9 shows the variation of ϵ_c with $\bar{\Phi}_0$ for investigated radial clearances, measured at two radial measurement locations: $r/b = 0.93$ and $r/b = 1$. In all instances, data for the Baseline configuration are reproduced for comparison.

Figure 9(a) shows the impact of modifying Clearance A. The reduction of this outermost radial clearance improves sealing performance across both measurement locations and for all examined purge mass flow rates. A significant benefit is realized at $r/b = 1$, as demonstrated in Table 2, where $\bar{\Phi}_{0,min}$ is reduced by 28%: defined as the purge mass flowrate required to achieve $\epsilon_c = 0.95$ at $r/b = 1$. Alternatively, if $\bar{\Phi}_{0,min}$ is equal to the value of $\bar{\Phi}_0$ corresponding to $\epsilon_c = 0.95$ at $r/b = 0.93 = c$, the parameter signifies sealing performance in the inner wheel-space. The reduction of Clearance A corresponds to a decrease of $\bar{\Phi}_{0,min}$ of 16% at $r = c$, with respect to the Baseline configuration. The relative improvement in sealing performance is greatest when in proximity to the clearance under consideration; this benefit diminishes in the inner wheel-space geometrically identical for $r/b \leq 0.93$.

Reducing Clearance A directly influences the impact of β_a upon the rim seal. A reduction of this radial clearance therefore increases $\partial V_\phi / \partial r$ across Clearance A. Considering an arbitrary fluid parcel at a constant radius, the reduction of Clearance A corresponds to an increase in the tangential velocity of the parcel resulting in a reduced swirl gradient across the rim seal. As a result, recalling Fig. 8, $\beta_c \Omega c$ is increased and hence ΔV_ϕ is reduced. Therefore, reducing the outermost radial clearance has the opposite effect of increasing C_F .

Sealing effectiveness at $r/b = 1$ was insensitive to Clearance A when it was increased with respect to the Baseline configuration (Fig. 9(a)). Considering the inner wheel-space however ($r/b = 0.93$), the clearance change resulted in a reduction in local sealing performance, where $\bar{\Phi}_{0,min}$ was increased by 9% compared to the Baseline configuration. This suggests that a relaxation of Clearance A enables deeper penetration of annulus gas into the cavity, while consequently diminishing the purge-mainstream swirl gradient.

Fluctuations in accordance with an intensified purge-mainstream shear gradient, resulting from a concomitantly maximized ΔV_ϕ and minimized r_m at the highest considered purge flow rates, led to incomplete sealing at the outermost measurement location. This phenomenon is observed to a lesser extent when Clearance A is reduced due to the relatively small decrease in ΔV_ϕ at a constant $\bar{\Phi}_0$.

4.2.2 Variation of Radial Extent of Axial Overlap. Figure 9(b) presents an independent variation of the inner radial clearance between overlapping seal lips (Clearance B). Varying the inner clearance results in a general insensitivity in ϵ_c at the $r/b = 0.93$ measurement location, which is further demonstrated by values of $\bar{\Phi}_{0,min}$ in Table 2. At the $r/b = 1$ measurement location, ϵ_c is largely independent of modifications of the inner stator-side radial clearance across the range of examined $\bar{\Phi}_0$. Such an insensitivity demonstrates that rim seal performance is primarily governed by the outermost radial clearance and therefore the purge-mainstream swirl gradient. The rotor-side rim seal displacements constitute a significantly greater impact upon the sealing performance of the stage than the stator-side counterparts.

Slight variations in sealing performance exist at $r/b = 1$ with respect to the Baseline, whereby the increased Clearance B

configuration increases ε_c for $\bar{\Phi}_0 \leq 1.0$, occurring concurrently with the inner wheel-space becoming sealed. When $\bar{\Phi}_0 > 1.0$, reducing Clearance B results in an improvement in sealing performance across the range of examined $\bar{\Phi}_0$ in comparison to the Baseline case.

4.2.3 Compound Effects. Compound clearance changes were achieved through modifying the rotor-side geometry, enabling the displacement of Clearances A and B simultaneously. First, consider a combined reduction of Clearance A with an increase of Clearance B. In accordance with Fig. 9(a), a substantial improvement in $\bar{\Phi}_{0,\min}$ (Fig. 9(c)) was exhibited, equal to a 16% improvement compared to the Baseline configuration at $r/b = 1$. The relative increase in ε_c was diminished in comparison to that when Clearance B is maintained (Fig. 9(a)). This result demonstrates that Clearance B can impact the exchange of fluid across the rim seal; however, this effect is only observed when Clearance A is reduced.

The compound reduction of Clearance A reduces $\bar{\Phi}_{0,\min}$ by 6% at $r/b = 0.93$ (Fig. 9(c)) compared to the Baseline, a decrease in magnitude compared to when Clearance A was diminished in isolation from Clearance B. Although the compound geometry change acts to reduce the purge-mainstream swirl gradient, as Clearance B is increased the fluid decelerates ($\partial V_\phi / \partial r$ across Clearance B reduces), increasing $\Delta\beta$ and produces an increased $\bar{\Phi}_{0,\min}$. The relative $\bar{\Phi}_{0,\min}$ improvement not only demonstrates the importance of considering the entirety of the rim seal geometry, but also critically that rim seal performance is assessed over a range of potential clearance changes that may arise during an engine transient.

When the compound Clearance A is increased, $\bar{\Phi}_{0,\min}$ is 26% higher than the Baseline value at $r/b = 1$. This performance reduction propagates radially inboard where a 15% increase in $\bar{\Phi}_{0,\min}$ was measured at $r/b = 0.93$. Therefore, the configuration constitutes the worst performing clearance displacement analyzed within this study. Once more, this result conforms to the general conclusion that rim seal performance has a more substantial dependency upon rotor-side displacements compared to those on the stator side.

4.2.4 Influence Upon Unsteadiness. It has been demonstrated that the outermost radial clearance controls the ingress of annulus gas for the aeroengine representative geometry investigated within this study; a reconciliation between steady and unsteady characteristics now follows. Two purge flows were considered here, spanning the range of observed spectral activity for the Baseline configuration (Fig. 7), and therefore $\Delta\beta$.

Figure 10 presents the impact of rim seal radial clearance upon ensemble-averaged PSD at two values of $\bar{\Phi}_0$. Spectral activity, specifically the lower-frequency activity associated with the purge-mainstream swirl gradient, can be considered a function of

Clearance A. When Clearance A is reduced, an intensification of PSD of up to 67% compared to the Baseline configuration is observed at $\bar{\Phi}_0 = 0.40$ (Figs. 10(a) and 10(c)). A reduction of Clearance A has a direct effect upon $\Delta\beta$: reducing clearance minimizes the penetration of ingress, subsequently reducing r_m and therefore enlarging the purge-mainstream swirl gradient. Recalling the relative flow diagram presented in Fig. 8, an identical trend was observed considering the superposition of purge, which intensified $\Delta\beta$ in association with an increased radial purge mass flux. Therefore, it is demonstrated that independently increasing the purge mass flowrate or decreasing the controlling seal clearance exhibits a unified effect upon low-frequency spectral content.

The sensitivity of unsteadiness with $\bar{\Phi}_0$ presented in Fig. 7 demonstrated that PSD intensity is a function of the radial flux of purge in the rim seal. Therefore, comparing configurations at constant $\bar{\Phi}_0$ indicates the radial purge flux and hence the relative sealing effectiveness. A relationship is present between the onset of the outer wheel-space sealing, governed by $\bar{\Phi}_{0,\min}$ at $r/b = 0.93$ (Table 2) and a reduction of the low-frequency PSD region in Fig. 10. Physically, the condition at which PSD begins to decrease corresponds to the radial migration of the recirculation zone radially outboard of the measurement location. Therefore, such a reduction indicates the sealing of the inner cavity. This correlation is reflected in Figs. 10(a) and 10(c), where for $\bar{\Phi}_0 = 1.34$, and an isolated reduction of Clearance A results in a 32% PSD reduction compared to the compound reduction of Clearance A, reflecting the attainment of a sealed inner wheel-space at a smaller $\bar{\Phi}_0$. The unsteady characteristics concur with the sealing performance rankings described in Table 2.

Conversely, the enlargement of Clearance A results in a slight reduction of PSD, independent of Clearance B for $\bar{\Phi}_0 = 0.40$ (Fig. 10). The PSD rediscovers an invariance with respect to the Baseline configuration both in regard to magnitude and extent in the frequency domain for $\bar{\Phi}_0 = 1.34$. Critically, the homogeneous spectral activity as $\bar{\Phi}_0$ increases, remains in agreement with measurements of ε_c described in Fig. 9.

Figure 10(b) shows that spectral activity is independent of Clearance B across the range of examined $\bar{\Phi}_0$. Recalling Fig. 9(b), a general independence was also observed when considering sealing performance across the rim seal. The observed relationship between the low-frequency PSD region, shown to be a function of $\Delta\beta$, and ε_c acts to provide further evidence that ingress is driven by the purge-mainstream swirl gradient across the rim seal.

4.3 Dimensionality Reduction Through Isolating the Swirl Gradient. It has been demonstrated that the swirl gradient across the rim seal is dependent on the degree-of-freedom explored: C_F , $\bar{\Phi}_0$ and the rim seal geometry. The swirl gradient and sealing

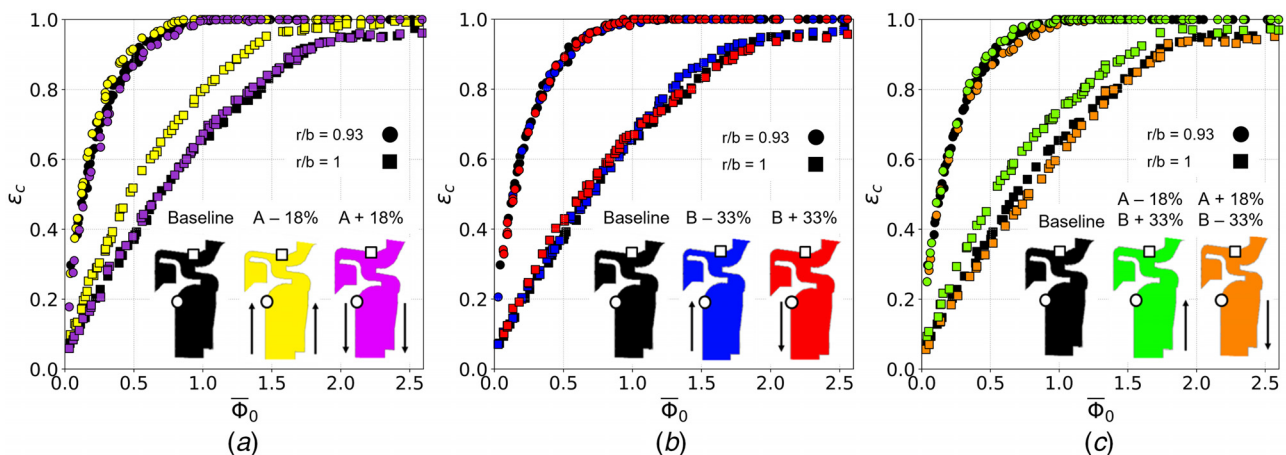


Fig. 9 ε_c versus $\bar{\Phi}_0$ curve for investigated radial clearances compared to the baseline configuration: (a) variation of clearance A, (b) variation of clearance B, and (c) compound clearance variation - clearance A and B simultaneously displaced

Table 2 Comparison of required purge mass flow to seal the wheel-space at $r/b=0.93$ and $r/b=1$ across examined configurations

Configuration	$\bar{\Phi}_{0,\min}$	
	($\varepsilon_c = 0.95$ at $r/b = 0.93$)	($\varepsilon_c = 0.95$ at $r/b = 1$)
Baseline	0.68	2.00
A-18%	0.57	1.45
A + 18%	0.74	2.00
B-33%	0.66	2.07
B + 33%	0.68	2.27
A-18%; B + 33%	0.64	1.69
A + 18%; B-33%	0.78	2.52

effectiveness are inextricably linked, a fact that can be exploited to simplify modeling approaches.

4.3.1 Varying β_a With Fixed β_c . As demonstrated in §4.1.1, the swirl gradient across the rim seal is altered by varying the C_F at a constant Φ_0 . To emphasize the governing nature of $\Delta\beta = \beta_a - \beta_c$, ε_c was multiplied by the according value of $\Delta\beta$ across the range of C_F , as shown in Fig. 11. β_a was estimated from isentropic velocity triangles, while $\beta_c \approx 0.4$ for all test cases. The invariance of $\varepsilon_c\Delta\beta$ with C_F provides significant evidence that ingress is governed by the purge-mainstream swirl gradient.

4.3.2 Varying β_c and Geometry With Fixed β_a . To highlight the relative dominance of $\Delta\beta$ as the primary driver for ingress, the inertial parameter Φ_0 was redefined to collapse data at $r/b = 1$. The generalized seal clearance parameter, s_c , was replaced by a weighted radial clearance, ζ , which defines the impact of the purge-mainstream swirl gradient across the rim seal—measured to vary in the interval: $0.87 \leq \Delta\beta \leq 1.22$ when increasing Φ_0 for the Baseline configuration (Fig. 7)

$$\Phi_{\Delta\beta} = \frac{\dot{m}_0}{2\pi\zeta\rho\Omega b^2} \quad (5)$$

where

$$\zeta = \overbrace{A(\beta_a - \beta_c)}^{\text{influence of } \Delta\beta \text{ governed by A}} = A\Delta\beta \quad (6)$$

A represents Clearance A, as defined in Fig. 3. An assumption is made that A governs the impact of the purge-mainstream swirl gradient. The variable ζ therefore governs the ingress potential for a constant \dot{m}_0 .

The definition of $\Phi_{\Delta\beta}$ in this way ensures that $\varepsilon_c \propto 1/\Delta\beta$, considering a constant \dot{m}_0 , as was demonstrated in §4.1.1. As \dot{m}_0 is increased the wheel-space pressurizes, leading to an inevitable increase in $\Delta\beta$ as previously shown in Fig. 7, and ultimately sealing the cavity.

In the wheel-space, the swirl in the core has been evaluated at the $r/b = 0.93$ measurement location on the stator wall; β_c is a function of both r/b and \dot{m}_0 . The empirical correlation derived by Dadkhah et al. [22] was used to describe the variation of the core tangential velocity in the wheel-space with \dot{m}_0

$$\frac{\beta}{\beta^*} = 0.087 \left[e^{5.2(0.486 - \lambda_T(r/b)^{-13/5})} - 1 \right] \quad (7)$$

where β^* is the value of β at the radial location of interest for $\bar{\Phi}_0 = 0$ and $\lambda_T = \left(\frac{\dot{m}_0}{\mu b}\right) Re_\phi^{-0.8}$.

The radial distribution of swirl was measured for all configurations including a variation of Clearance A; data were compared to predicted values from the empirical correlation [22], shown in Fig. 12(a). The free disk entrainment limit corresponds to $\lambda_T > 0.22$ ($\lambda_T[r/b]^{-13/5} > 0.27$) [23], beyond which the experimental data exhibit an increased deviation from the empirical correlation as core rotation suppresses and ultimately collapses.

$\Phi_{\Delta\beta}$ was then used to collapse data for the $r/b = 1$ measurement location. It is important to note that collapsing data at $r/b = 1$ are subject to the ε_c paradox that arises when considering alternative measurement locations across double seals [9]. Effectiveness data presented in Figs. 9(a) and 9(c) are collapsed upon $\Phi_{\Delta\beta}$. Consider first the case of varying the radial Clearance A (Fig. 12(b)). A collapse here demonstrates that the relative purge-mainstream swirl gradient acts as the principal driver for ingress and is governed by the outermost radial clearance. Second, when Clearances A and B undergo a compound variation, a collapse of ε_c is again obtained at the $r/b = 1$ location. Interestingly, configurations where Clearance A is increased in comparison to the Baseline, exhibit a departure from the collapsed curve (Fig. 12) when $0.05 \leq \Phi_{\Delta\beta} \leq 0.07$. This suggests the existence of a potential fluidic mechanism that

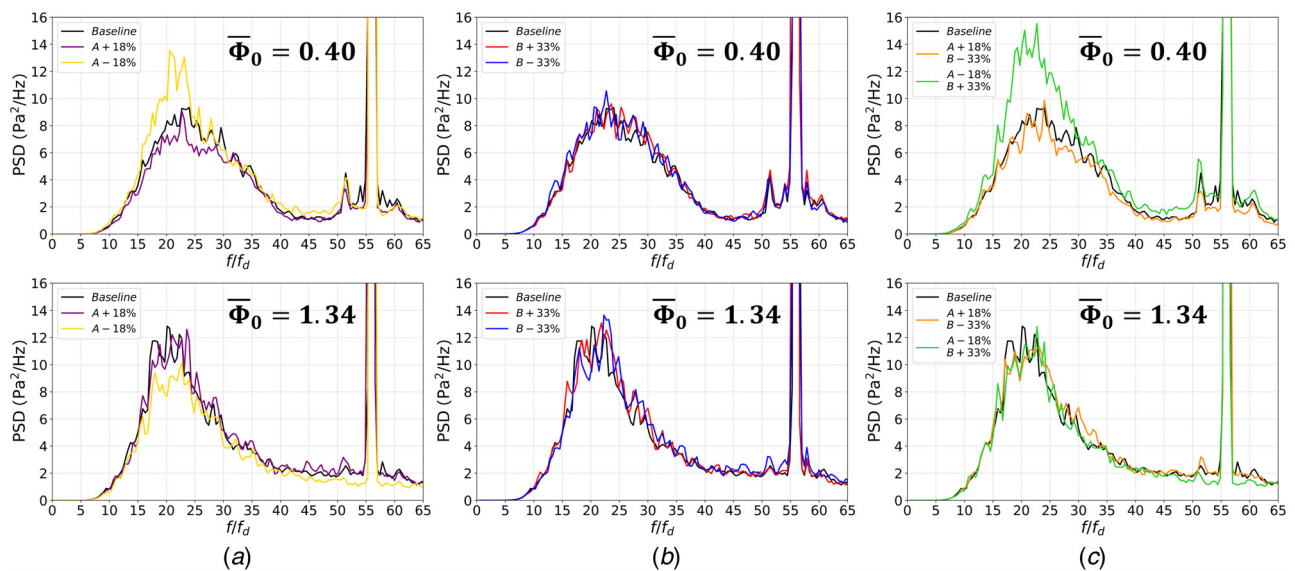


Fig. 10 Impact of seal configuration upon ensemble-averaged spectral activity at on-design conditions for $\bar{\Phi}_0=0.40$ and $\bar{\Phi}_0=1.34$: (a) variation of clearance A, (b) variation of clearance B, and (c) compound clearance variation - clearance A and B simultaneously displaced

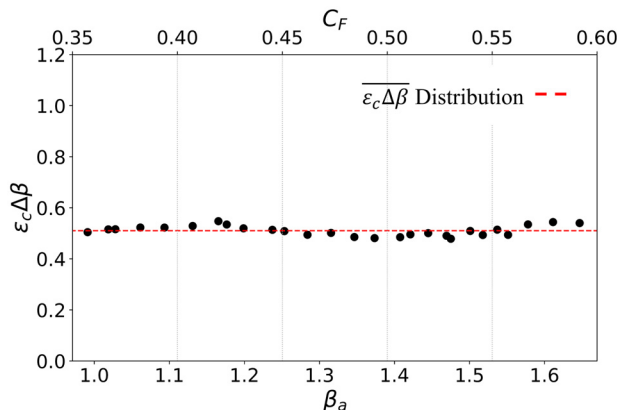


Fig. 11 C_F sweep (at $r/b = 1$) for a constant $\bar{\Phi}_0 = 0.67$ for the Baseline configuration. The standard deviation of $\varepsilon_c \Delta\beta = 0.0194$.

suppresses the impact of $\Delta\beta$ and prevents the ingestion of further annulus gas.

Variations in spectral activity, when Clearance A was altered, were attributed to differing radial purge mass fluxes, as shown in Fig. 10. For the case of $\Phi_{\Delta\beta} = 0.036$ and consequently $\varepsilon_c \approx 0.61$, PSD is shown to collapse for all configurations where Clearance A is varied, as demonstrated in Fig. 13. Universality in the distribution of PSD corresponds to an invariance in the radial flux of purge and hence $\Delta\beta$. Therefore, a cause-and-effect relationship is presented between the purge-mainstream swirl gradient and heightened spectral activity. Critically, a relationship is established between steady sealing performance and the unsteady pressure spectrum.

4.4 Implications for Aeroengine Design. Rim seal performance is largely insensitive to any isolated stator-side seal lip displacement, which in the context of this study governs Clearance B (Fig. 9(b)). However, rotor-side displacement (i.e., thermal expansion or centrifugal loading effects), which lead to variations in Clearance A were proven to have a substantial impact upon sealing performance (Figs. 9(a) and 9(c)), especially in close proximity to the annulus. Minimizing Clearance A was shown to reduce $\Phi_{0,\min}$ by 16% and 28% considering an aeroengine representative geometry and characteristic radii of $r/b = 0.93$ and $r/b = 1$, respectively.

Dimensionality reduction of ε_c can be attained through isolating the purge-mainstream swirl gradient. Collapsing data upon $\varepsilon_c \Delta\beta$ suggest that if $\Delta\beta$ is characterized across a range of C_F conditions,

effectiveness data obtained at a single Φ_0 and C_F condition can be used to predict effectiveness for all C_F .

Conditions with varying radial purge mass flux (i.e., varying (Φ_0)) were collapsed using $\Phi_{\Delta\beta}$ across a range of seal configurations. An injective function between ε_c and the superposed flowrate was derived, from which measurements of PSD were shown to unify the steady and unsteady sealing characteristics. Critically, it was shown that the spectral content within an unsteady pressure trace could be used to indicate sealing performance.

5 Conclusions

The impact of parameters influencing ingress is generally well-established in the steady sense; however, much uncertainty remains over the spectral characteristics of ingress, which have been addressed within this study. A combination of time-averaged and unsteady measurements was utilized to assess the impact of C_F , Φ_0 and the influence of radial clearance changes. This paper reports the relationship between time-averaged and unsteady rim seal characteristics, addressing a fundamental gap in the literature.

Key conclusions from the study are as follows:

- For a fixed Baseline geometry and Φ_0 , measurements of time-averaged swirl and sealing effectiveness have demonstrated that sealing effectiveness is inversely proportional to the purge-mainstream swirl gradient across the rim seal. Ensemble-averaged PSD derived from unsteady pressure measurements for a range of C_F conditions exhibited a persistence frequency contribution ($10 \leq f/f_d \leq 45$) across all examined C_F , coupled with its proportionality to $\Delta\beta$, identifies the former as a principal driver for ingress.
- When considering the Baseline geometry at a fixed C_F and a range of Φ_0 , measurements demonstrated an enlargement of the purge-mainstream swirl gradient as Φ_0 was increased and core rotation suppressed. $\Delta\beta$ is shown to be a function of the radial extent of annulus gas penetration. Derived PSD at discrete values of Φ_0 exhibited increased intensity as more superposed flow was applied, a similar effect to that observed when increasing C_F .
- By modifying the inner and outer radial clearance of an aeroengine representative double lip rim seal, measurements of ε_c across a range of Φ_0 and fixed C_F demonstrated that reducing the outermost clearance produced the greatest reduction in $\Phi_{0,\min}$ (28% compared to the Baseline configuration). For each configuration, a direct comparison between the PSD and sealing performance was produced. Best performing configurations exhibited elevated PSD for lower purge flows, associated with an increased radial purge flux and therefore improved sealing.

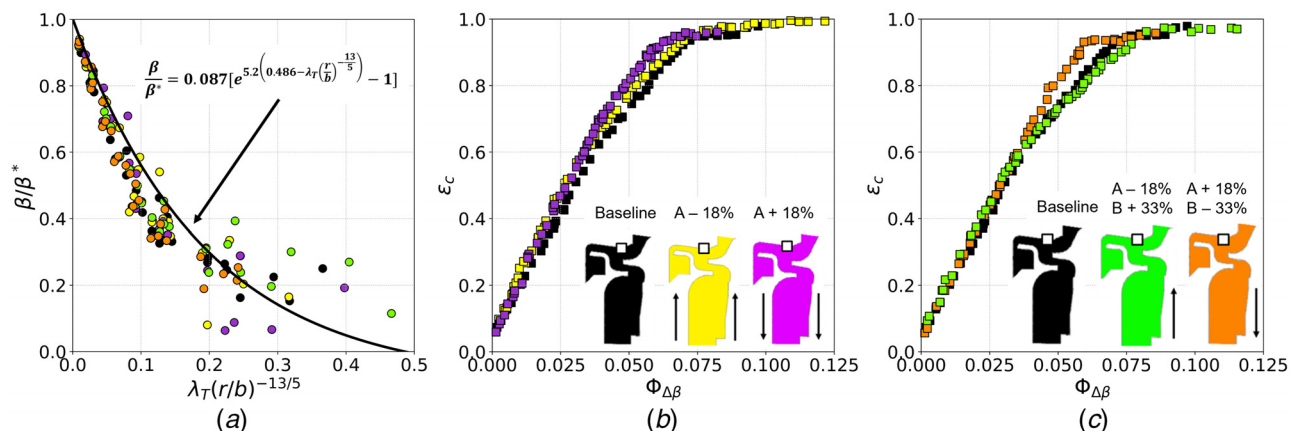


Fig. 12 (a) Variation in the relative tangential velocity of the wheel-space core ($0.4 \geq r/b \geq 0.93$) for all configurations where Clearance A is modified, (b) collapse upon swirl when Clearance A is varied at $r/b = 1$, and (c) collapse upon swirl for case of compound seal clearance at $r/b = 1$

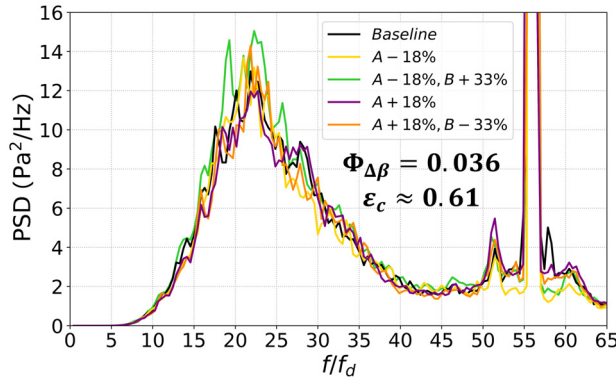


Fig. 13 Collapsed spectral activity for $\Phi_{\Delta\beta} = 0.036$ and $\varepsilon_c \approx 0.61$ when clearance A is varied. Φ_0 is in the range 0.67–0.93.

- Dimensionality reduction through isolating the purge-mainstream swirl gradient resulted in an invariant distribution of $\varepsilon_c \Delta\beta$ with C_F . Furthermore, assuming that the outer seal clearance governs the purge-mainstream swirl gradient, the parameter $\Phi_{\Delta\beta}$ was found to collapse ε_c data for all rim seal configurations across a range of superposed flow conditions. An injective function associating \dot{m}_0 with ε_c demonstrated that the distribution of PSD is preserved for conditions of constant ε_c .

Acknowledgment

The authors would like to acknowledge the technical expertise and support of Andrew Langley and Sam L'esteve who enabled the continued running of the experimental facility and its instrumentation. The authors would also like to thank Safran Aircraft Engines, especially Clément Jarrossay, Damien Bonneau, and Fatoumata Bintou Santara for their close collaboration and for providing an industrial perspective to this study, in addition to funding this work in its entirety.

Data Availability Statement

Due to confidentiality agreements with research collaborators, supporting data can only be made available to bona fide researchers subject to a nondisclosure agreement. Details of how to request access are available at the University of Bath data archive.

Nomenclature

Roman Letters

- a = reference radius for annulus ($r/b = 1.04$) (m)
- A = outermost radial clearance (clearance A) (m)
- b = radius of seal (m)
- B = inner radial clearance (clearance B) (m)
- c = reference radius for inner wheel-space ($r/b = 0.93$) (m)
- c_a = concentration of tracer gas in the annulus (%)
- c_s = local concentration of tracer gas (%)
- c_0 = concentration of tracer gas in the purge flow (%)
- C_F = flow coefficient ($= W/\Omega b$)
- C_P = pressure coefficient ($= \frac{p - p_{ref}}{\frac{1}{2}\rho\Omega^2 b^2}$)
- C_2 = absolute vane exit velocity (m/s)
- f = measured frequency (Hz)
- f_d = frequency of disk rotations (Hz)
- M = Mach number
- \dot{m}_0 = purge mass flow rate (kg/s)
- \dot{m}_A = annulus mass flow rate (kg/s)
- p = static pressure (Pa)
- p_{baro} = barometric (atmospheric) pressure (Pa)
- p_{inlet} = inlet pressure (Pa)
- p_t = total pressure (Pa)

$p_{unsteady}$ = time-resolved pressure fluctuations (Pa)

r = radius (m)

r_m = medial length associated with ingress penetration across rim seal (m)

Re_w = axial Reynolds number in annulus based on radius ($= \rho W b / \mu$)

Re_ϕ = rotational Reynolds number ($= \rho \Omega b^2 / \mu$)

s_c = rim gap clearance (m)

S_c = local seal clearance (m)

T_A = annulus temperature (K)

T_{ws} = wheel-space temperature (K)

V_ϕ = tangential velocity (m/s)

W = axial velocity (m/s)

Greek Symbols

β = swirl ratio ($= V_{\phi\infty}/\Omega r$)

β_a = swirl ratio in the annulus at $r = a$

β_c = swirl ratio in the inner wheel-space at $r = c$ (evaluated at $r/b = 0.93$)

β^* = swirl ratio for $\dot{m}_0 = 0$ kg/s

$\Delta\beta$ = swirl difference ($= \beta_a - \beta_c$)

$\widetilde{\Delta\beta}$ = swirl gradient ($= \Delta\beta/\Delta r$)

ε_c = concentration effectiveness

λ_T = turbulent flow parameter ($= \left(\frac{\dot{m}_0}{\mu b}\right) Re_\phi^{-0.8}$)

μ = dynamic viscosity (kg/ms)

ρ = density (kg/m³)

Φ_0 = non-dimensional sealing parameter ($= \frac{\dot{m}_0}{2\pi s_c \rho \Omega b^2}$)

$\Phi_{0,min}$ = value of Φ_0 required for $\varepsilon_c = 0.95$ at measurement location

$\Phi_{0,min}^*$ = value of Φ_0 required for $\varepsilon_c = 1$ at $r/b = 0.93$

Φ_0 = normalized non-dimensional sealing parameter

($= \Phi_0/\Phi_{0,min}^*$)

$\Phi_{\Delta\beta}$ = swirl gradient based non-dimensional sealing parameter

($= \frac{\widetilde{\Delta\beta}}{2\pi\zeta\rho\Omega b^2}$)

ζ = effective seal clearance governed by annulus swirl

($= A[\beta_a - \beta_c] = A\Delta\beta$) (m)

Appendix: Uncertainty Analysis

Experimental uncertainty propagation has been quantified through the use of the Taylor Series Method for the reduction of equations. Table 3 presents measurement uncertainty for variables described in this work. Table 4 outlines the accuracy of the instrumentation utilized.

To demonstrate the Taylor Series Method procedure, an uncertainty calculation for the nondimensional purge flowrate (Φ_0) is described.

Φ_0 is equal to

$$\Phi_0 = \frac{\dot{m}_0 R T_{ws}}{2\pi s_c (p_{baro} + p_{inlet}) \Omega b^2} \quad (A1)$$

Ignoring uncertainties in geometric quantities

$$\left(\frac{\delta\Phi_0}{\Phi_0}\right)^2 = \left(\frac{\delta\dot{m}_0}{\dot{m}_0}\right)^2 + \left(\frac{\delta T_{ws}}{T_{ws}}\right)^2 + \left(\frac{\delta\Omega}{\Omega}\right)^2 + \frac{\delta p_{baro}^2 + \delta p_{inlet}^2}{(p_{baro} + p_{inlet})^2} \quad (A2)$$

Table 3 Derived estimated measurement uncertainty

Quantity	Uncertainty
$\delta C_F / C_F$	3.0%
$\delta \Phi_0 / \Phi_0$	1.5%
$\delta C_P / C_P$	3.5%
$\delta \beta / \beta$	1.2%
$\delta \varepsilon_c / \varepsilon_c$	2.3%

$$\bar{\Phi}_0 = 0.93, C_F = 0.51, Re_\phi = 8.9 \times 10^5.$$

Table 4 Instrumentation accuracy

X_i	δX_i	Range
c_s, c_a, c_0	$\pm 1\%$ FS	0–1% CO ₂
\dot{m}_A	$\pm 3\%$ of reading	0–0.7 kg/s
\dot{m}_0	$\pm 0.2\%$ ^a FS	0–0.073 kg/s
p_{baro}	$\pm 0.5\%$ of reading	954–1073 mbar
p_{inlet}	$\pm 0.5\%$ FS	0–50 mbar
p_s, p_t	$\pm 0.06\%$ FS	0–70 mbar
T_A, T_{ws}	± 0.5 K	278–303 K
$p_{unsteady}$	$\pm 0.03\%$ ^a FS	0–350 mbar
Ω	± 1 rpm	0–3500 rpm

^aTrue accuracy derived from calibration curve.

References

[1] Cao, C., Chew, J. W., Millington, P. R., and Hogg, S. I., 2004, "Interaction of Rim Seal and Annulus Flows in an Axial Flow Turbine," *ASME J. Eng. Gas Turbines Power*, **126**(4), pp. 786–793.

[2] Savov, S. S., Atkins, N. R., and Uchida, S., 2017, "A Comparison of Single and Double Lip Rim Seal Geometries," *ASME J. Eng. Gas Turbines Power*, **139**(11), p. 112601.

[3] Monge-Concepción, I., Siroka, S., Berdanier, R. A., Barringer, M. D., Thole, K. A., and Robak, C., 2021, "Unsteady Turbine Rim Sealing and Vane Trailing Edge Flow Effects," *ASME Paper No. GT2021-59273*.

[4] Rozman, M., DeShong, E. T., Thole, K. A., Berdanier, R. A., and Robak, C., 2023, "Characterizing Flow Instabilities During Transient Events in the Turbine Rim Seal Cavity," *ASME J. Turbomach.*, **145**(3), p. 031014.

[5] Berg, R. A., Tan, C. S., Ding, Z., Laskowski, G., Palafox, P., and Miorini, R., 2018, "Experimental and Analytical Assessment of Cavity Modes in a Gas Turbine Wheel-space," *ASME J. Eng. Gas Turbines Power*, **140**(6), p. 062502.

[6] Hösgen, T., Meinke, M., and Schröder, W., 2020, "Large-Eddy Simulations of Rim Seal Flow in a One-Stage Axial Turbine," *J. Global Power Propul. Soc.*, **4**, pp. 309–321.

[7] Bru Revert, A., Beard, P. F., and Chew, J. W., 2023, "Measurement of Inertial and Acoustic Waves in a Turbine Chute Rim Seal Cavity," *ASME J. Eng. Gas Turbines Power*, **145**(6), p. 061021.

[8] Gao, F., Chew, J. W., and Marxen, O., 2020, "Inertial Waves in Turbine Rim Seal Flows," *Phys. Rev. Fluids*, **5**(2), p. 024802.

[9] Sangan, C. M., Pountney, O. J., Scobie, J. A., Wilson, M., Owen, J. M., and Lock, G. D., 2013, "Experimental Measurements of Ingestion Through Turbine Rim

Seals—Part III: Single and Double Seals," *ASME J. Turbomach.*, **135**(5), p. 051011.

[10] Popović, I., and Hodson, H. P., 2013, "The Effects of a Parametric Variation of the Rim Seal Geometry on the Interaction Between Hub Leakage and Mainstream Flows in High Pressure Turbines," *ASME J. Eng. Gas Turbines Power*, **135**(11), p. 112501.

[11] Daniels, W. A., Johnson, B. V., Graber, D. J., and Martin, R. J., 1992, "Rim Seal Experiments and Analysis for Turbine Applications," *ASME J. Turbomach.*, **114**(2), pp. 426–432.

[12] Burden, S., Chew, J. W., Gao, F., and Marxen, O., 2024, "Effect of Rim Seal Geometry on Rotationally-Driven Ingestion," *ASME J. Eng. Gas Turbines Power*, **146**(9), p. 091013.

[13] Graikos, D., Tang, H., Sangan, C. M., Lock, G. D., and Scobie, J. A., 2022, "A New Interpretation of Hot Gas Ingress Through Turbine Rim Seals Influenced by Mainstream Annulus Swirl," *ASME J. Eng. Gas Turbines Power*, **144**(11), p. 111005.

[14] Choi, M., Goo, B., Cho, G., and Song, S. J., 2024, "Swirl Enhancement Effect on Turbine Rim Seal Performance," *ASME J. Turbomach.*, **146**(5), p. 051002.

[15] Cong, Q., Lei, L., Zhang, K., Li, Z., and Li, J., 2023, "Effect of Inflow Swirl on the Sealing Effectiveness of Turbine Rim Seal," *ASME Paper No. GT2023-102768*.

[16] Vella, S., Darby, P., Carnevale, M., Scobie, J. A., Lock, G. D., Jarrossay, C., Salvatori, F., Bonneau, D., and Sangan, C. M., 2024, "A Combined Experimental and Turbulence-Resolved Modeling Approach for Aeroengine Turbine Rim Seals," *ASME J. Eng. Gas Turbines Power*, **146**(8), p. 081020.

[17] Camci, C., Averbach, M., and Town, J., 2019, "Unsteady Flow Structures Within a Turbine Rim Seal Cavity in the Presence of Purge Flow—an Experimental and Computational Unsteady Aerodynamics Investigation," *Aerospace*, **6**(5), p. 60.

[18] Daubechies, I., and Bates, B. J., 1993, "Ten Lectures on Wavelets," *J. Acoust. Soc. Am.*, **93**(3), p. 1671.

[19] Welch, P., 1967, "The Use of Fast Fourier Transform for the Estimation of Power Spectra: A Method Based on Time Averaging Over Short, Modified Periodograms," *IEEE Trans. Audio Electroacoust.*, **15**(2), pp. 70–73.

[20] Graikos, D., Carnevale, M., Sangan, C. M., Lock, G. D., and Scobie, J. A., 2021, "Influence of Flow Coefficient on Ingress Through Turbine Rim Seals," *ASME J. Eng. Gas Turbines Power*, **143**(11), p. 111010.

[21] Bailly, C., and Comte-Bellot, G., 2015, *The Dynamics of Isotropic Turbulence*, Springer International Publishing, Cham, pp. 179–210.

[22] Dadkhah, S., Turner, A. B., and Chew, J. W., 1992, "Performance of Radial Clearance Rim Seals in Upstream and Downstream Rotor–Stator Wheel-spaces," *ASME J. Turbomach.*, **114**(2), pp. 439–445.

[23] Owen, J. M., and Rogers, R. H., 1989, *Flow and Heat Transfer in Rotating-Disc Systems*, Mechanical Engineering Research Studies, Vol. 1, Research Studies Press Ltd., Taunton, UK.